Joule

CellPress

Article

A Superionic Conductive, Electrochemically Stable Dual-Salt Polymer Electrolyte

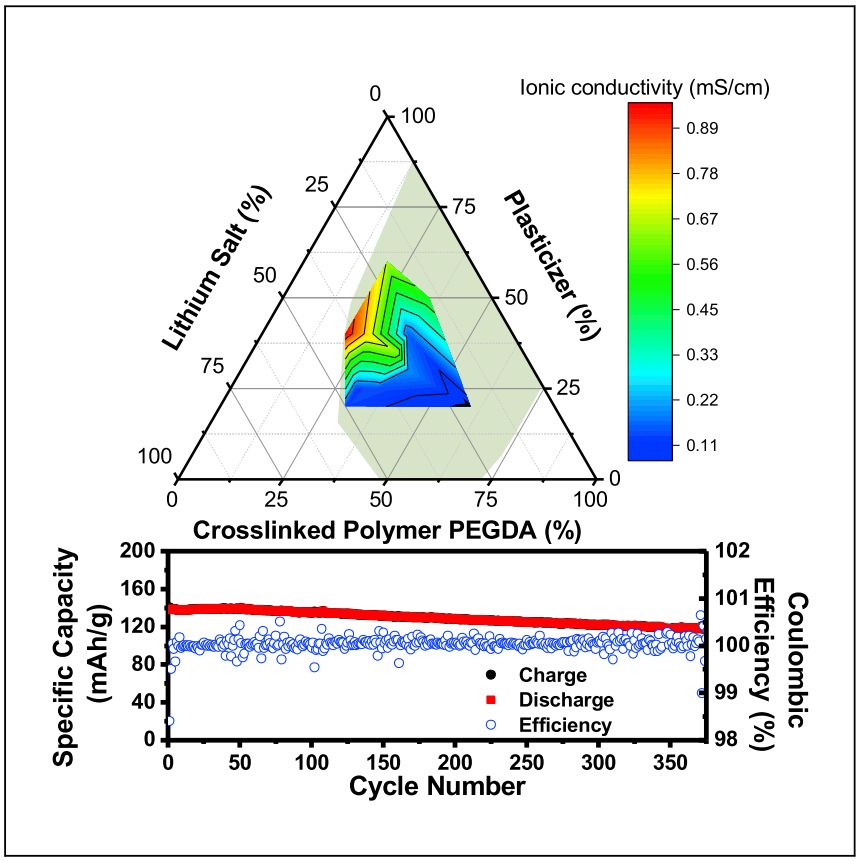

The ternary phase diagrams were used to guide the design of polymer electrolyte composites. The dual-salt LiTFSI/LiBOB polymer electrolyte with optimized ionic conductivity over 1.0 mS/cm at 30°C was achieved in the isotropic phase. The lithium metal cells with free-standing polymer electrolyte exhibited outstanding average coulombic efficiency of 99.99% in the first 370 cycles, with a capacity retention of 86%.

Si Li, Yu-Ming Chen, Wenfeng Liang, Yunfan Shao, Kewei Liu, Zhorro Nikolov, Yu Zhu

yu.zhu@uakron.edu

HIGHLIGHTS

Polymer electrolytes with superionic conductivity (1.0 mS/cm) at RT

Phase diagram approach for searching highly ionic conductive polymer composites

Dual-salt polymer electrolytes with outstanding electrochemical stability

All solid-state batteries with average coulombic efficiency over 99.99%

Li et al., Joule 2, 1–19
September 19, 2018
https://doi.org/10.1016/j.joule.2018.06.008

Please cite this article in press as: Li et al., A Superionic Conductive, Electrochemically Stable Dual-Salt Polymer Electrolyte, Joule (2018), https://doi.org/10.1016/j.joule.2018.06.008

Joule

CellPress

Article

A Superionic Conductive, Electrochemically Stable Dual-Salt Polymer Electrolyte

Si Li,[1,2] Yu-Ming Chen,[1,2] Wenfeng Liang,[1] Yunfan Shao,[1] Kewei Liu,[1] Zhorro Nikolov,[1] and Yu Zhu[1,3,*]

SUMMARY

A phase diagram-guided rational design was introduced to fabricate polymer composite electrolyte, avoiding Edisonian investigations in searching for a polymer electrolyte with high ionic conductivity. The free-standing, flexible, dual-salt-based polymer electrolyte films with superionic conductivity (1.0 mS/cm) at 30°C have been demonstrated. The synergistic effect of salts gave the dual-salt polymer electrolyte outstanding electrochemical stability with a wide electrochemical window of 0–4.5 V (versus Li/Li$^+$). The lithium stripping/plating experiments indicated that the polymer electrolyte could be safely cycled under current density from 0.05 to 0.5 mA/cm^2. The dual-salt polymer electrolyte-based cells exhibited excellent average coulombic efficiency of ~99.99% in the first 370 cycles. The initial capacity at 30°C is 138 mAh/g (0.2 C), which is close to the value achieved by liquid-electrolyte-based cells under similar condition. The capacity retention is 86% after 370 cycles, indicating the long-term stability of the polymer electrolyte.

Context & Scale

Solid-state electrolytes (SSEs) are crucial for developing safe lithium metal anode-based batteries. Among available SSEs, the solid polymer electrolyte (SPE) sub-category is of particular interest due to the flexibility and low fabrication cost of polymeric materials. However, conventional SPEs have low ionic conductivity and thus are not used in commercial lithium ion batteries. The search for optimized SPE is challenging and often relies on the researchers' experience. In this work, a rational ternary phase diagram approach was used to avoid Edisonian trial-and-error investigations in searching for ionic conductive polymer composites. Free-standing, flexible polymer electrolyte films with superionic conductivity were demonstrated. By combining a multiple lithium salts design, the polymer electrolyte exhibited outstanding electrochemical stability in battery tests. The method developed in this work paves a way to design novel SPEs for advanced lithium metal anode batteries.

INTRODUCTION

Lithium ion batteries (LIBs) have become one of the technological advancements that are inseparable from our daily lives. Valuable features such as long cycle stability, high power, and energy density are being pursued in order to further extend the usage time for portable electronics and electric vehicles.[1,2] Several incidents related to battery failure, presumably due to lithium dendrite formation that eventually led to thermal runaway, raised safety concerns about the commercial liquid electrolyte used in LIBs,[3] as the organic carbonate-based electrolytes have potential hazard-prone properties, including high volatility and no mechanical strength.[4–6] The demand for a safer electrolyte will become no less critical to the next-generation lithium batteries where lithium metal electrode will be utilized: lithium metal has been regarded as the potential negative electrode for future LIBs[7–9] and is used as the electrode in advanced lithium cells[10] such as lithium-sulfur[11] and lithium-air[12] batteries. These novel high-energy-density, high-power-density lithium metal electrode-based batteries require a safer electrolyte to replace the carbonate-based liquid electrolytes. Solid-state electrolyte (SSE) is one of the promising candidates to not only provide high lithium ionic conductivity but also to achieve a safer battery due to its all-solid-state nature.[13–19] Among available SSEs, the solid polymer electrolyte (SPE) sub-category is of particular interest due to the flexibility of polymeric materials and low fabrication cost. The discovery and subsequent development of SPE was initiated in 1975 when poly(ethylene oxide) (PEO) was combined with alkali metal salt complexes to provide measurable ionic conductivity.[20] However, it was until 1979 that an SPE was reported to be utilized in LIBs.[21] Other than PEO, many

other polymers, including poly(acrylonitrile) (PAN),[22–24] poly(methyl methacrylate) (PMMA),[25,26] poly(vinylidene fluoride) (PVDF),[27] and poly(vinyl chloride) (PVC),[28,29] were proposed as the host or to be combined with different polymers for the salt component. Nonetheless, as of now, PEO is still the most studied and researched host polymeric system. PEO, with the characteristic oxyethylene (CH_2–CH_2–O) repeating units, has strong solvating properties for a great variety of salts through the interaction of ether oxygens with cations.[30] In addition, it was also reported that PEO is highly efficient in coordinating metal ions due to orientation and optimal distance of the ether oxygen atoms in polymer chains.[31] The utilization of binary SPEs (PEO/salt) could yield ionic conductive composites, in which systems the ionic conductivity was determined by the competition between lattice energy and solvation energy of polymer host and salt.[32] PEO was found to form complexes with many lithium salts, such as LiCl, $LiClO_4$, LiBr, LiI, LiSCN, $LiBF_4$, $LiAsF_6$, and $LiCF_3SO_3$.[33] However, due to the semicrystalline structure of pristine PEO, the PEO-based binary SPEs were found to exhibit relatively low ionic conductivity[34,35] of 10^{-3} to 10^{-2} mS/cm at room temperature, which was not practical for LIB applications.[36]

In the traditional description of ionic conductive processes in SPE, the lithium ions within the local polymer segments dissociate and recombine at sequential coordination sites.[37] It was generally believed that the ion transport occurred in the amorphous phase[38] and the crystalline regions of the SPE hindered the migration of ions,[39] despite other conduction mechanisms being reported otherwise.[40] Therefore, many techniques were developed in order to enhance the amorphousness of the SPE and thus improve the ionic conductivity of the SPEs. Plasticization, where an organic compound possessing high dielectric constant was added to the polymer host,[41–43] was commonly employed to increase the ionic conductivity of the SPE by increasing amorphousness without elevating the temperature. Common organic liquid plasticizers including ethylene carbonate (EC),[41] propylene carbonate (PC),[43] and dimethyl carbonate (DMC)[43] applied into the SPE typically result in the formation of gel-like electrolytes. A special class of plasticizers was plastic crystal materials such as succinonitrile (SN). SN was solid and was demonstrated to form superionic conductive plastic crystalline solid with lithium salt.[44] Previous work demonstrated that integration of plastic crystalline SN could produce self-standing SPEs with good ionic conductivities.[45,46] Other than the amorphousness of the SPE, the aforementioned PEO-salt complexes suffered from low cation transport number, which could result in the deterioration of electrodes.[47] Thus, in order to improve the transport number while interfering with the crystallization process of the PEO chains, salts with large anions could be introduced to the SPE.[45] The bis(trifluoromethane) sulfonamide lithium salt LiTFSI emerged as arguably the best salt for PEO-based polymer electrolytes. Owing to the very low lattice energy, LiTFSI had high solubility and was one of the most dissociated salts.[48–51] However, LiTFSI was not applied in conventional liquid-electrolyte-based LIBs due to the severe corrosive effect on aluminum collectors. In previous reports,[52] LiTFSI-based polymer electrolytes showed limited cycle performance and low coulombic efficiency in cell testing.

Herein, a novel dual-salt-based polymer electrolyte is reported. The electrolyte was prepared from LiTFSI, lithium bis(oxalate)borate (LiBOB), glutaronitrile (GN) plastic crystal, and poly(ethyleneglycol) diacrylate (PEGDA) prepolymer hosts. The low molecular weight of PEGDA allowed complete mixing with salt and plastic crystals. Through a crosslinking reaction, a free-standing SPE was achieved. By using ternary phase diagram analysis, a dual-salt SPE (DS-SPE) with superionic conductivity (1.0 mS/cm) at 30°C was obtained. Electrochemical and thermal characterizations were carried out to determine the stability of the free-standing and solvent-free

[1]College of Polymer Science and Polymer Engineering, University of Akron, Akron, OH 44325, USA

[2]These authors contributed equally

[3]Lead Contact

*Correspondence: yu.zhu@uakron.edu

https://doi.org/10.1016/j.joule.2018.06.008

Please cite this article in press as: Li et al., A Superionic Conductive, Electrochemically Stable Dual-Salt Polymer Electrolyte, Joule (2018), https://doi.org/10.1016/j.joule.2018.06.008

SPE. Electrochemical performance evaluation of LIBs of Li/SPE/$LiFePO_4$ demonstrated that the novel polymer electrolyte exhibited excellent electrochemical stability during long cycle testing.

RESULTS AND DISCUSSION

Ternary Phase Diagram-Guided SPE Development

By eliminating the crystalline phase of the polymer and dissociation of lithium salt, the ionic conductivity of polymer composites could reach the maximum. However, the search for an optimized combination of different components in polymer electrolytes has often been based on the researchers' experience. In this work, a rational ternary phase diagram approach was used to avoid Edisonian trial-and-error investigations in searching for ionic conductive polymer composites.[52] Samples with different concentrations of PEGDA, GN, and lithium salt were prepared and used to study the crystalline and isotropic phase of the composite. The composite was mounted on a glass slide and then placed under a polarized optical microscope to observe the morphology of the composite at different temperatures. The results are shown in Figure 1. As shown in Figures 1A–1F, three morphologies were observed in the composite at different temperatures: (1) the isotropic phase represented the amorphous state of the mixture, which is presented as the red dots (experimental data) and shadowed area on the phase diagram. The isotropic phase was more desirable for high ionic conductivity. (2) Lithium salt crystal phase existed through the entire temperature range when the salt concentration was high, and it expanded as the temperature decreased. The segregated lithium salt crystal affected free-standing SPE film formation, and hence should be avoided. (3) The PEGDA crystal phase was evident at low temperature. Although low-molecular-weight PEGDA was amorphous at room temperature, it crystallized at low temperature (−10°C) when the concentration of PEGDA in the composite was high. The spherulites formed in Figure 1D indicated the formation of typical semicrystalline polymer. The formation of polymer crystal will suppress the chain segment motion, leading to a low ionic conductivity. The ternary phase diagram provided a design scheme for achieving high ionic conductivity in the SPE. As batteries needed to be operated at different temperatures, the overlap of isotropic phase regions at different temperatures defined the composition range where the SPE should be prepared.

The low-molecular-weight PEGDA was liquid at room temperature. In order to form a free-standing SPE film, PEGDA must be cured to form crosslinked solid polymer. In this work, the free-standing SPE was fabricated by mixing a PEGDA prepolymer host, lithium salt, plasticizer, and photoinitiator into a transparent liquid prior to the UV-induced photopolymerization (see Experimental Procedures). The ternary phase diagram of crosslinked SPE was studied using similar methods and the results are shown in Figures 1G–1I. It was evident that crosslinked PEGDA had a smaller polymer crystal region (the crosslinked PEGDA crystal is shown in Figure S1), which was expected since the crystallization process was suppressed in the crosslinked polymer network. It was also found that the free-standing SPE film could not be formed when the PEGDA ratio was low (indicated as the orange points). The film with low PEGDA content was gel-like. Across three different temperatures (the phase diagrams at 25°C and 75°C are almost identical), the shadowed region on the phase diagram indicated the composition range where the free-standing SPE film with an isotropic phase should be formed. Combining the ternary phase diagrams based on PEGDA/plasticizer/lithium salt and crosslinked SPE, the "working area" of ionic conductive SPE was determined (Figure 1). An illustration of free-standing SPE is

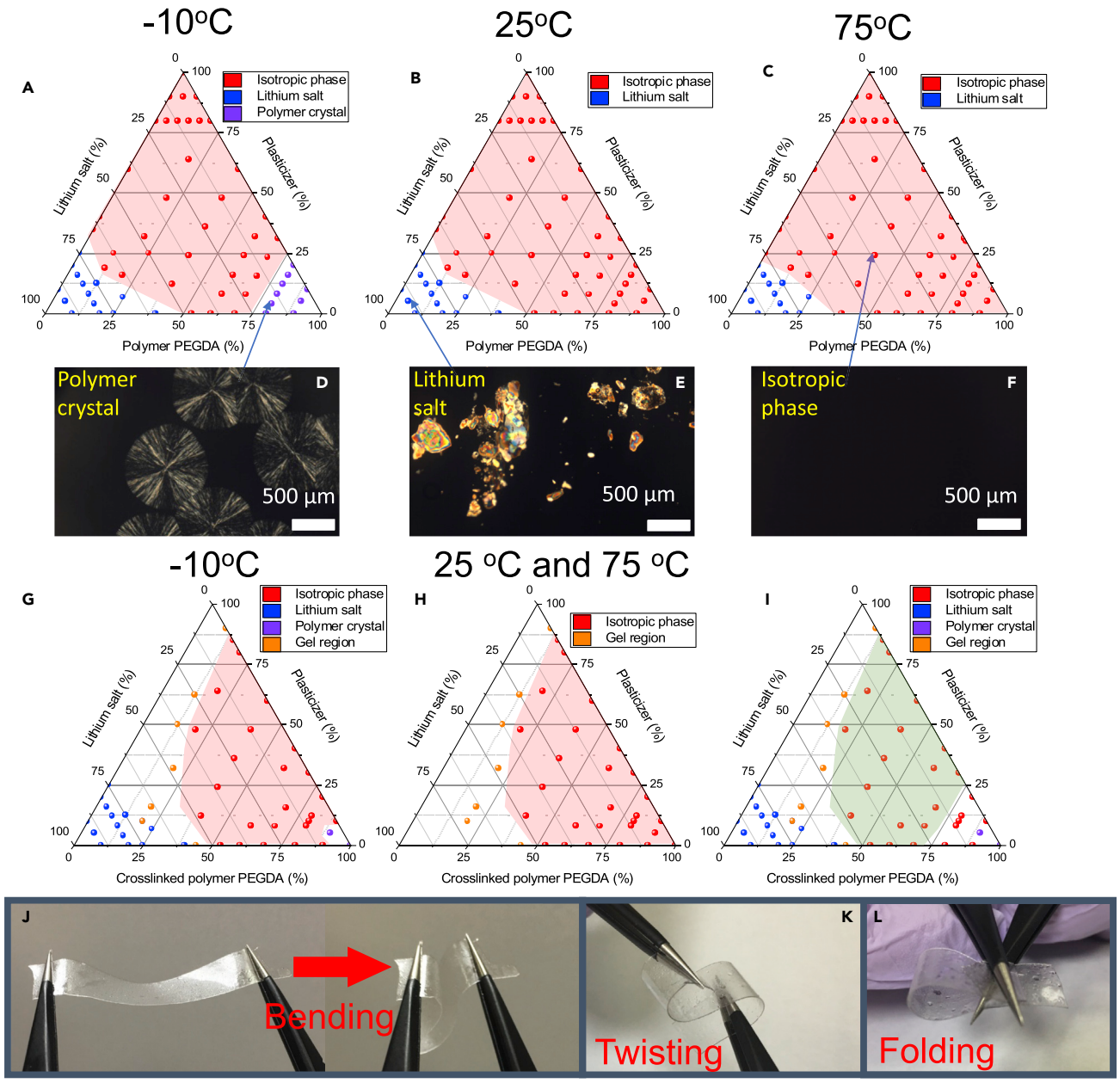

Figure 1. Phase Diagram of Polymer Composite Electrolyte

(A–C) Ternary phase diagrams of PEGDA/lithium salt/plasticizer at the temperatures (A) −10°C, (B) 25°C, (C) and 75°C based on the polarized optical microscopy image characterization. Red points, isotropic phase; blue points, lithium salt; purple points, polymer PEGDA crystal. The shadowed area, which is drawn manually for clarity, indicates the isotropic phase range.

(D–F) Polarized optical microscopy images corresponding to (D) polymer PEGDA crystal, (E) lithium salt crystal, and (F) isotropic phase.

(G and H) Ternary phase diagrams of crosslinked PEGDA/lithium salt/plasticizer at different temperatures (−10°C, G; 25°C and 75°C, H) based on the polarized optical microscopy image characterization. Orange points, gel region.

(I) The ternary phase diagram with marked region (green) where the free-standing isotropic SPE can be created.

(J–L) The picture of SPE film demonstrating the (J) flexibility, (K) twistability, and (L) foldability.

shown in Figures 1J–1L, demonstrating that the SPE possessed good flexibility and bendability. Such a flexible SPE provided sufficient mechanical strength, preventing the direct contact between the cathode and the anode during cell fabrication. Although the free-standing SPE film could be made as thin as 68 µm by the

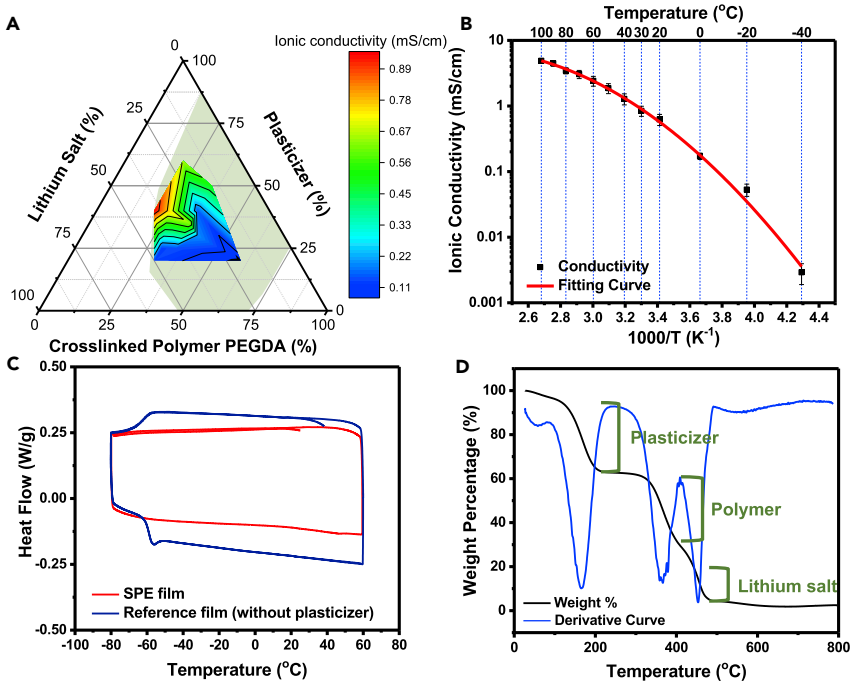

Figure 2. Characterization of Polymer Composite Electrolyte

(A) The ionic conductivity (at 20°C) of SPE on the ternary phase diagram. The green shadowed region is the suggested isotropic phase region for SPE film fabrication based on the phase diagram analysis.

(B) The temperature-dependent ionic conductivity of the SPE (crosslinked PEGDA/plasticizer/lithium salt = 35:35:30).

(C) The DSC thermogram of the SPE film (red line, crosslinked PEGDA/plasticizer/lithium salt = 35:35:30) and the reference film without plasticizer (blue line, crosslinked PEGDA/lithium salt = 35:30).

(D) The TGA thermogram of the SPE (crosslinked PEGDA/plasticizer/lithium salt = 35:35:30).

blade-coating method (Supplemental Information Figure S2), to ensure proper handling in cell fabrication, thicker SPE films (250–1,000 μm) prepared by molds of different sizes were used in the electrochemical experiments conducted in the following sections.

SPE Characterization

Ionic conductivity was generally regarded as the most important parameter for SPE. The free-standing isotropic SPE films prepared on the basis of ternary phase diagram analysis were studied for the lithium ionic conductivities by the electrochemical impedance spectroscopy (EIS) method followed by the calculation of the equation below:

$$\sigma = \frac{l}{R_b \cdot A}$$

where σ was the ionic conductivity, l was the thickness, R_b was the bulk resistance, and A was the area of the SPE. The ionic conductivities of different samples at 20°C were measured and the conductivity gradient was plotted in Figure 2A. It showed that ionic conductivity of SPE reached the highest values at the ratio of 25:40:35 (crosslinked PEGDA/plasticizer/lithium salt) and 35:35:30. The highest average ionic conductivities were 0.76 mS/cm (25:40:35) and 0.62 mS/cm (35:35:30) at 20°C. The phase-diagram-guided conductivity optimization method

Please cite this article in press as: Li et al., A Superionic Conductive, Electrochemically Stable Dual-Salt Polymer Electrolyte, Joule (2018), https://doi.org/10.1016/j.joule.2018.06.008

not only provided the optimized composition for ionic conductivity but also revealed the trend of conductivity change across individual components.

The SPE's conductivity exhibited a temperature-dependent behavior, as shown in Figure 2B. The increase in ionic conductivity as the temperature increases could be ascribed to the higher chain mobility, which can be plotted following the Vogel-Tamman-Fulcher empirical formula[43,47]:

$$\sigma = \sigma_0 \cdot T^{-\frac{1}{2}} \exp\left(-\frac{E_a}{k_B(T - T_0)}\right)$$

where σ_0 was the pre-exponential factor that was related to number of charge carriers, k_B was the Boltzmann constant, E_a was the pseudo-activation barrier related to critical free volume for ion transport, and T_0 was the reference temperature, typically 10–50 K below the glass transition temperature (T_g). The results are shown in Table S1 and the curve is plotted in Figure 2B. In Figure 2B, the transition point was not observed until the temperature dropped to −20°C, which was consistent with the ternary phase diagram analysis. At 30°C, the average ionic conductivity was 0.84 mS/cm and the sample with the highest conductivity reached 1.0 mS/cm. The average ionic conductivity dropped to 0.2 mS/cm at 0°C and increased to 4.9 mS/cm at 100°C. The comparison of the ionic conductivity performance of the SPE is shown in Figure S3.

The crystallinity and amorphousness nature of the SPE were further evaluated by differential scanning calorimetry (DSC) measurements, as shown in Figure 2C. In order to eliminate possible residual water in the sample, samples were dried overnight in a vacuum oven before the DSC measurement. It was reported[53] that the polymerized PEGDA had a glass transition temperature ranging between −40°C and −30°C. As shown in Figure 2C, the glass transition temperature of pure crosslinked PEGDA was found to be around −50°C. This glass transition was absent in the DSC thermograms when plasticizer was incorporated in the SPE, which indicated that the ternary system had a significantly decreased glass transition temperature, leading to an enhancement in chain mobility and ionic conductivity. In addition to DSC measurements, thermal stability of the SPE was tested utilizing thermogravimetric analysis (TGA). In Figure 2D, the TGA thermograms show the thermal stability of individual components in the SPE. The SPEs were stable up to approximately 100°C without significant deterioration, suggesting that the SPE film could be utilized at elevated temperatures up to 100°C. The initial weight loss corresponded to the decomposition of the plastic crystal GN, where a ~35% weight loss was observed. In comparison with the commonly employed organic carbonate-based electrolytes that exhibited poor thermal stability below 100°C,[54] the SPE film could serve as an alternative to provide a safer barrier against conditions at higher temperatures. Subsequent decompositions starting at 300°C and 350°C corresponded to the polymer and lithium salt, respectively, which was coherent with the initial mixing ratio.

The lithium ion transference number (t_{Li}^+) is the ratio of lithium ion transport to the total ion transport contributed from both cations and anions. A transference number of unity implies the ion transport was contributed solely by the targeted ion, which is highly desirable for LIB applications. Low t_{Li}^+ led to ionic concentration gradients within the battery, which induced undesirable side reactions, and high internal and interfacial resistances, and therefore hindered the performances. The t_{Li}^+ of the SPE could be obtained by methods of direct current (DC) polarization combined with EIS, known as the AC (alternating current)/DC method.[55] The

Please cite this article in press as: Li et al., A Superionic Conductive, Electrochemically Stable Dual-Salt Polymer Electrolyte, Joule (2018), https://doi.org/10.1016/j.joule.2018.06.008

values obtained from the method could then be calculated by the following equation:

$$t^+ = \frac{I_{ss}(V - I_0 R_0)}{I_0(V - I_{ss} R_{ss})}$$

where V was the polarization potential that was applied onto the cell, I_0 and I_{ss} were defined as the initial and steady-state currents, and R_0 and R_{ss} were the initial and steady-state interfacial resistances before and after the polarization. In Figure S4, the AC impedances (shown in the inset) and the DC polarization curve are shown. The calculated t_{Li}^+ for the SPE was approximately 0.75, which was significantly higher than that of conventional liquid electrolytes. Typical liquid electrolytes usually exhibited a t_{Li}^+ of less than 0.5 due to solvation.[56] The high t_{Li}^+ from the SPE could be ascribed to the entrapment of the large bis(trifluoromethane) sulfonamide anions within the polymer network matrices, allowing the lithium ions to be the single conducting species.

Electrochemical Stability Characterization

In order to galvanostatically charge/discharge a battery cell, the SPE should possess sufficient electrochemical stability to prevent side reactions arising between the interface of SPE and electrode. Linear sweep voltammetry (LSV) and cyclic voltammetry (CV) were conducted to evaluate the electrochemical stability of the SPE. The LiTFSI/LiBOB dual-salt system exhibited an overall better electrochemical stability than the LiTFSI single-salt system. In Figures 3A and 3B, the major oxidative degradation of SPE was initiated at voltages above 5 V (versus Li/Li^+). However, there was a small oxidation peak around 4.3 V in the single-salt system, indicating the possible oxidative degradation of the single-salt SPE (SS-SPE) system at the relatively low voltage. Further CV evaluation on the oxidation and reduction was carried out from −0.5 to 4.8 V with the same scanning rate as the LSV, which is illustrated in Figures 3C and 3D. The symmetric peak from −0.5 to 0.5 V was ascribed to the lithium stripping/plating on the stainless steel (StSt) electrode.[57] The reduction and oxidation peaks remained at the same position after several cycles, indicating the lithium stripping/plating process was a reversible process. It was evident that the addition of LiBOB salt rendered a better stability at the higher voltage. From both the LSV and the CV, it could be observed that, upon oxidation at the beginning of 4 V, the SPE with single LiTFSI salt exhibited small current response, whereas the SPE with the dual salt remained flat and stable up to 4.5 V. At 1 V, a few small peaks corresponded to the reduction of organic compounds on the lithium metal electrode. The LiTFSI/LiBOB dual-salt system suppressed the reduction reaction compared with the LiTFSI single-salt system. The results were similar (Figure S5) to the phenomenon observed recently in a liquid electrode with the LiTFSI/LiBOB dual-salt system on the lithium metal electrode, where a stable interface on the lithium metal electrode was formed.[58]

Prior to assessing the SPE films in actual batteries with pure lithium metal, the lithium stripping/plating electrochemical characterization was conducted using a symmetric lithium cell with the configuration of Li|SPE|Li. The charge and discharge time protocols were fixed at 1.5 hr with a specific current density of 0.05 mA/cm^2. The performance of the lithium stripping/plating using the DS-SPE is shown in Figure 3E (similar stripping/plating test results of SS-SPE are shown in Supplemental Information Figure S6.), where the stripping/plating process exceeded 1,300 hr, demonstrating the durability and electrochemical stability of the SPE. The stripping/plating at 200–250 cycles and 1,200–1,250 cycles are shown in Figures 3F and 3G, respectively. Similar voltage profiles indicated that the SPE was stable during the long cycle experiment. The

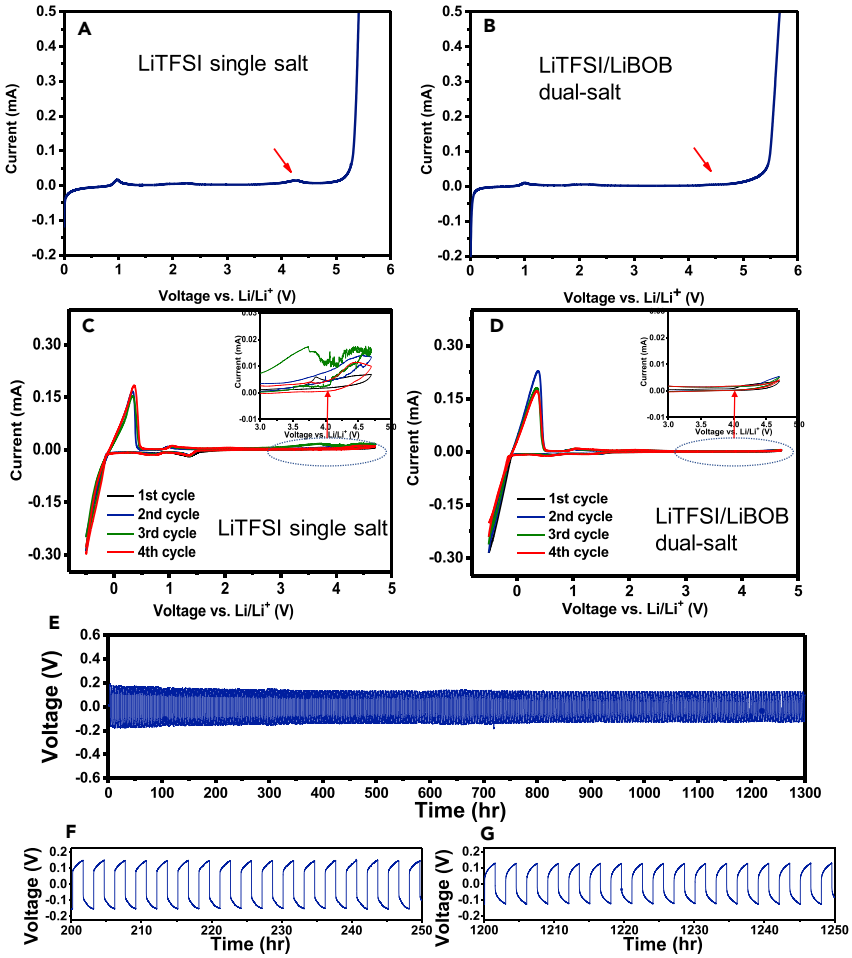

Figure 3. Electrochemical Stability Tests

(A and B) LSV of the single-salt (LiTFSI) SPE (A) and LSV of the dual-salt (LiTFSI/LiBOB) SPE (B). The LSV indicates that there is a small oxidation peak around 4.3 V (indicated by the red arrow) in the single-salt system.

(C) CV of the single-salt (LiTFSI) SPE. The inset is the enlarged figure at the high-voltage region.

(D) CV of the dual-salt (LiTFSI/LiBOB) SPE. The inset is the enlarged figure at the high-voltage region. It is clear from the inset and figure that the DS-SPE has a better electrochemical stability at the high-voltage region.

(E–G) Lithium stripping/plating test conducted at a current density of 0.05 mA/cm^2: (E) voltage profile over the entire stripping/plating test, (F) voltage profile between the 200th and 250th hr, and (G) voltage profile between the 1,200th and 1,250th hr. The charge and discharge time were fixed at 1.5 hr.

stripping/plating tests of DS-SPE at higher current density are shown in Figure S7. The results indicated the DS-SPE film was stable at current density of 0.5 mA/cm^2. The morphology of the lithium metal electrodes after cycling was studied. In Supplemental Information Figure S8, scanning electron microscopy images of lithium electrodes cycled in the SPE cell and the liquid cell are compared with pristine lithium foil. As shown in Figures S8A and S8B, both deposited lithium (light part) and lithium foil substrate (dark part) were visible. In comparison with Figure S8B, the contrast of the deposited lithium in Figure S8A to the substrate lithium foil was lower, suggesting a thinner layer of deposited lithium and better dendrite mitigation in the SPE cell. The stripping/plating electrochemical characterization demonstrated the capability of the SPE to mitigate the shorting of the cell by the lithium dendrite.[59]

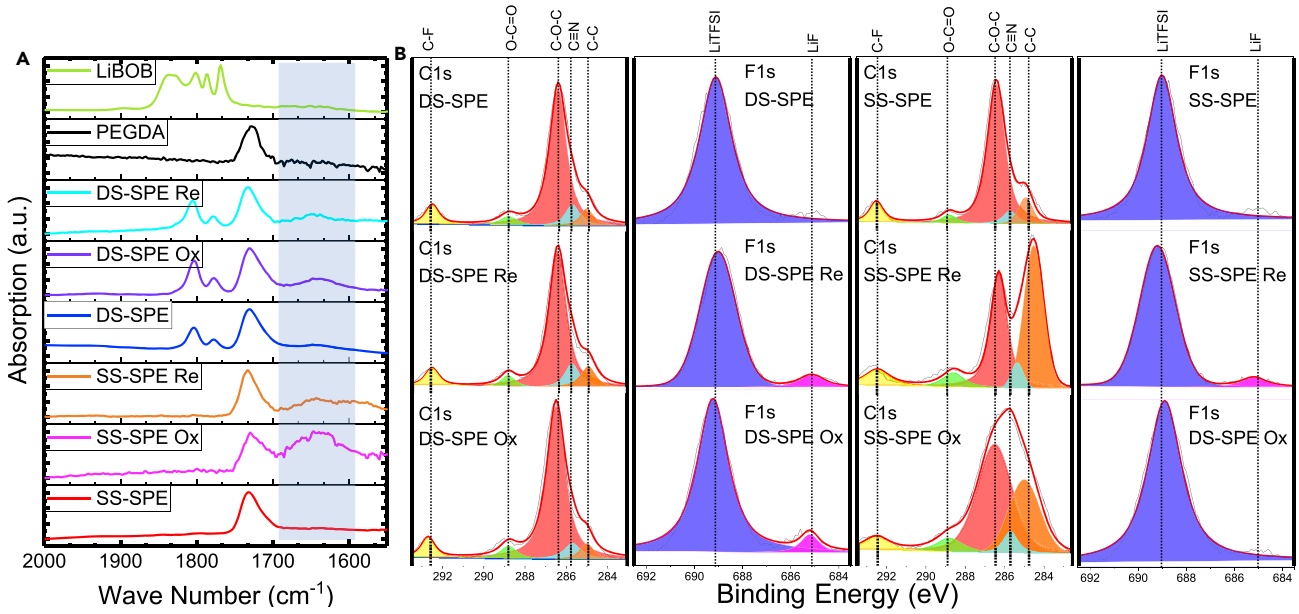

Figure 4. ATR-FTIR and XPS Characterization

(A) ATR-FTIR characterization of SS-SPE and DS-SPE. The FTIR spectra were collected under reductive (Re)/oxidative (Ox) and neutral conditions. The FTIR of LiBOB and PEGDA are listed for comparison. The spectra at wave number range of 1,550–2,000 cm^{-1} are shown. The full range of FTIR spectra and additional references are listed in Supplemental Information Figure S9.

(B) XPS characterization of the dual-salt and SS-SPEs under neutral, oxidative, and reductive conditions. C1s and F1s spectra are listed. For C 1s spectra, the spectra are deconvoluted into an orange peak corresponding to hydrocarbon (C–H/C–C, 285.0 eV), a cyan peak corresponding to cyano group (C≡N, 285.7 eV), a red peak corresponding to ether carbon (C–O–C, 286.4 eV), a green peak corresponding to ester carbonyl group (O–C=O, 288.8 eV), and a yellow peak corresponding to carbon-fluorine bond (C–F, 293.2 eV). For F1s spectra, the spectra were deconvoluted into a blue peak corresponding to LiTFSI (C–F, 689.1 eV) and a magenta peak corresponding to LiF (Li–F, 685.2 eV).

The enhanced electrochemical stability was further investigated by the attenuated total reflection (ATR)-Fourier-transform infrared spectroscopy (FTIR) and X-ray photoelectron spectroscopy (XPS) study. Similar StSt|SPE|Li blocking cells were used in the tests. To study the oxidative state, the cells were scanned from 0 V to 5 V (versus Li/Li^+) under LSV with the scan rate of 0.5 mV/s. When the voltage reached 5 V, the cells were disconnected and disassembled inside the glove box. The SPE films were removed from cells and characterized by FTIR and XPS, noted as the oxidized form (Ox). For the SPE samples under the reductive state, the blocking cells were tested under CV within the voltage range of −0.5–4.8 V (versus Li/Li^+) for two cycles and then stopped at 0.5 V (scan rate, 0.5 mV/s). The cells were then disassembled and the SPE films were characterized, noted as the reduced form (Re). The untreated SPE films were also characterized and all results are listed in Figure 4 and Supplemental Information Figure S9.

Figure 4A and Supplemental Information Figure S9 show ATR-FTIR results of SS-SPE, DS-SPE films, and references including untreated SPE, PEGDA, lithium salts, and plasticizer. The full ATR-FTIR spectra of all materials are shown in Supplemental Information Figure S9. Figure 4A shows the FTIR spectra in the region of 1,550–2,000 cm^{-1}, where the strong signals related to the carbonyl group are recorded. As shown in Figure 4A, untreated SPEs (both SS-SPE and DS-SPE) exhibited an infrared (IR) absorption ~1725 cm^{-1} that originated from PEGDA. For DS-SPE, there were two additional peaks between 1775 and 1825 cm^{-1}, which were from LiBOB. Under oxidative state, the single-salt film (SS-SPE Ox) showed a broad peak at 1,600–1,700 cm^{-1}, indicating the formation of new carbonyl groups. The IR signal

Please cite this article in press as: Li et al., A Superionic Conductive, Electrochemically Stable Dual-Salt Polymer Electrolyte, Joule (2018), https://doi.org/10.1016/j.joule.2018.06.008

intensity of new carbonyl groups was even stronger than that of the original peak derived from PEGDA, suggesting a significant oxidation process on the polymer. A similar broad peak was observed from SS-SPE under reductive state (SS-SPE Re in Figure 4A). The reductive state was achieved by CV cycles, in which the SPE films were cycled (from 0 V to 5 V, versus Li/Li^+) twice before they were kept at reductive potential (0.5 V versus Li/Li^+). The emerged carbonyl signals could be formed by a similar mechanism when the cells were cycled; i.e., the parasitic oxidative side reactions of polymer matrix could be responsible for the formation of new peaks and lead to poor electrochemical stability of SS-SPE. For the DS-SPE, there was only an insignificant bump peak at 1,630 cm^{-1} on FTIR spectra after oxidation/reduction, suggesting a much more stable polymer matrix with the existence of LiBOB.

XPS further elucidated those changes. As shown in Figure 4B, carbon C1s and fluorine F1s spectra were investigated. In C1s spectra, hydrocarbon (C–C/C–H, 285.0 eV),[60] cyano group (C≡N, 285.7 eV),[61] ether group (C–O–C, 286.4 eV),[62] ester carbonyl group (O–C=O, 288.8 eV),[62] and carbon-fluorine bond (C–F, 293.2 eV)[63] could be assigned. After the oxidation scan/reduction scan, no obvious peak shifts or changes were observed in DS-SPE C1s spectra, revealing the stable nature of DS-SPE. For SS-SPE, however, significant electronic structure changes of carbon were observed. In the untreated SS-SPE C1s spectrum, ether group (C–O–C, 286.4 eV) was the major form. Under oxidized state, the peak around 286.4 eV was significantly broadened. Such a broadened peak could be ascribed to the formation of new bonds such as aldehyde/ketone carbonyl groups (C=O, ~ 287.3 eV) and carbon hydroxyl bonds (C–OH, ~ 285.8 eV).[64] Another significant change under oxidized state was the increase and expansion of hydrocarbon bonds (C–C/C–H, 285.0 eV), which indicated the formation of more hydrocarbon bonding states (eg, C–H, C–C, C=C) Based on those observations, the degradation of SS-SPE at high voltage could be ascribed to the ether bond cleavage. A possible process was described as the following: typical ether bonding cleavage was a nucleophilic attack process, where the ether oxygen atom lost one electron and formed corresponding carbocation species.[65] The electrochemical oxidation could assist this process by removing the electron from the ether oxygen atom electrochemically. The cleavage of ether bonds resulted in alcohols and alkenes.[66] The alcohols could be further oxidized into aldehyde/ketone[67] as the electrochemical voltage is applied. The proposed process explained the observed expanded peak around 286.4 eV where the aldehyde/ketone carbonyl group (C=O, ~ 287.3 eV) and carbon hydroxyl bond (C–OH, ~ 285.8 eV) were expected. The formation of alkene also matched well with the observation of the increased and expanded hydrocarbon bond signals (~285.0 eV). In addition, new carbonyl signals in ATR-FTIR spectra could be correlated with the formation of aldehyde/ketone.

The reductive SS-SPE C1s spectrum also showed a significant increase of hydrocarbon bond signals (~285.0 eV) compared with untreated SS-SPE. Compared with C1s spectrum of oxidative SS-SPE, the reductive SS-SPE exhibited a narrower band around 286.4 eV and the peak of this band was shifted slightly to lower binding energy direction, which could be explained as the aldehyde/ketone reduction, shifting the C1s signals to the alcohol's carbon.

The drastically different degradation phenomena of SS-SPE and DS-SPE might originate from the passivation layer formed at the interface of SPE and electrodes. As shown in the F1s XPS, a significant Li-F peak (685.2 eV) was observed throughout the oxidation and reduction of DS-SPE, which could be associated with the formation of a LiF-containing passivation layer on the SPE surface during scans. LiF was

reported[68,69] as a favorable lithium conducting species in solid electrolyte interlayers (SEI) in commercial LIB anodes. As for the SS-SPE, weak Li-F signal was observed only on the reductive electrode. It was expected the drastic polymer degradation under oxidative conditions might prevent the formation of a stable LiF-containing passivation layer, leading to the worse overall electrochemical stability.

The EIS data of the symmetrical cells before and after the stripping/plating experiments confirmed the formation of a passivation interlayer between lithium metal electrode and DS-SPE. As shown in Supplemental Information Figure S10, the bulk resistance (R_b) did not change significantly over time. However, the charge transfer resistance (R_{ct}) increased initially and stabilized after ~50 hr. The results indicated an interlayer formed between the lithium metal and SPE, similar to the SEI observed on the LIB anode.[68,69]

Lithium Metal Battery Fabrication and Testing

Unlike the liquid electrolyte, contacting the active material, solid electrolyte, and carbon filler was crucial for a solid electrolyte-based LIB.[70] Although the magnitude and origin of the interfacial resistance for polymer electrolytes remained a controversial issue,[71,72] the general concept to mitigate the interfacial resistance was to increase the deformability of the electrolyte to facilitate conformal contact with other components in a similar manner as their liquid analogs. Such a conformal contact with active materials and carbon filler was particularly important on the cathode side, where the lithium metal oxides usually had low intrinsic conductivity. The free-standing solid electrolyte film could only work well with cathodes that had low active mass loading. A composite cathode (i.e., mixing the solid electrolyte, active materials, and carbon fillers) was required. In this work, the precursor polymer electrolyte (including low-molecular-weight prepolymer PEGDA, lithium salt, and plasticizer) was infiltrated into the casted cathode materials. Due to the low molecular weight of the non-crosslinked PEGDA, the electrolyte was a viscous liquid that could be integrated with active materials. The infiltrated electrode was then laminated with free-standing SPE film (250 μm) and photo-crosslinked, resulting in a robust composite electrode. Figure 5A shows the lithium metal battery fabrication procedure using the SPE. The electrode/electrolyte interface is shown by scanning electron microscopy imaging (Figure 5B).

Lithium iron phosphate ($LiFePO_4$ [LFP]) was used as the cathode material and presoaked in the non-crosslinked SPE overnight so that the electrolyte could infiltrate thoroughly. Figure 6A showed galvanostatic charge/discharge cycles of the LFP cathode with the SPE. The first nine cycles (not shown in Figure 6A) were operated in the range of 2.5–3.7 V to ensure the formation of stable SEI layers on both the lithium metal and LFP cathode.[73] The initial discharge capacity showed a specific charge capacity of about 120 mAh/g at a current density of 0.2 C. The coulombic efficiency fluctuated in the first few cycles and eventually stabilized toward a value of >99.5% in subsequent cycles, suggesting that a stable interfacial layer on both the anode and cathode side have been formed. After the initial nine cycles, the chemical window was further extended to 2.5–3.9 V to fully release specific capacity within the LFP cathode at the same current density, where specific capacities of ~138 mAh/g could be achieved. This value was comparable with liquid electrolyte results (Figure S11) using the same electrode materials. The battery exhibited an average coulombic efficiency of 99.99% through the following cycles. The specific capacity at its 200th cycle still exhibited a value of ~128 mAh/g, which was ~93% in capacity retention. A detailed comparison of the DS-SPE and SS-SPE is shown

Please cite this article in press as: Li et al., A Superionic Conductive, Electrochemically Stable Dual-Salt Polymer Electrolyte, Joule (2018), https://doi.org/10.1016/j.joule.2018.06.008

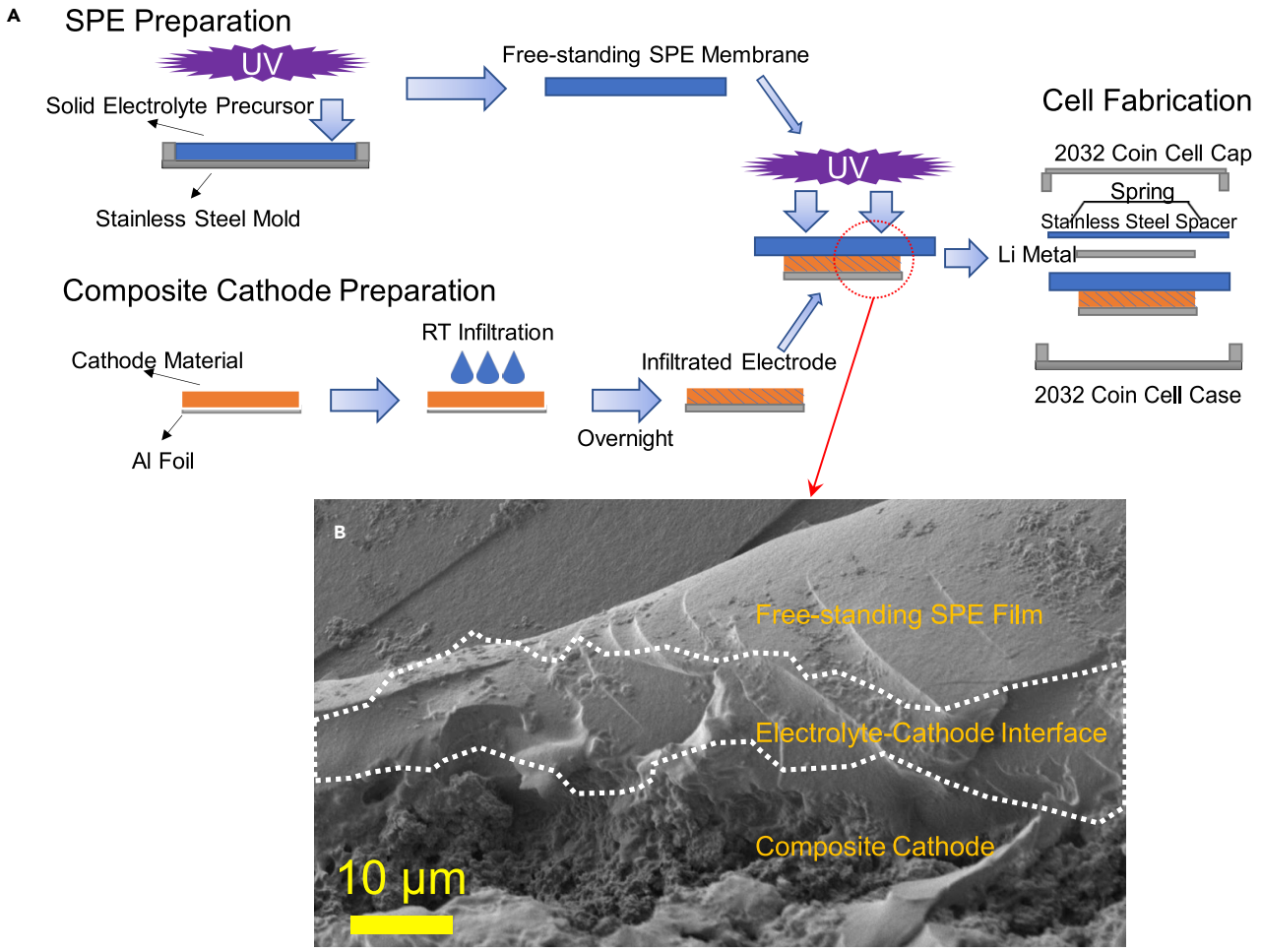

Figure 5. SPE Film and Composite Cathode Fabrication

(A) Scheme of free-standing SPE film fabrication, composite cathode preparation, and battery assembly. RT, room temperature.

(B) Scanning electron microscopy image of cross section of the fabricated SPE film and composite electrode.

in Figure S12. The cell with SS-SPE (LiTFSI) had capacity retention of 82% after 200 cycles (Figure S12A). As shown in Figure S12A, the specific capacity faded rapidly and started to severely fluctuate from ~55th cycle, indicating the deterioration of the SS-SPE. The coulombic efficiency of SS-SPE-based battery also fluctuated more compared with DS-SPE-based battery (Figures S12A and S12B). The specific capacity of the DS-SPE-based battery at its 370th cycle still exhibited a value of ~118 mAh/g, which was 86% in capacity retention. The overall better stability of DS-SPE could be ascribed to the synergistic effect of LiBOB and LiTFSI salt: the LiBOB salt passivated aluminum well at high potentials,[74,75] serving as an ideal co-salt for LiTFSI. LiTFSI mitigated the reaction of LiBOB with lithium metal electrode, improving the stability of SPE over the lithium electrode.[58] Figure 6B showed the representative charge/discharge profiles at different cycles. Compared with conventional LFP cell in liquid electrolyte, the SPE cell showed a more obvious polarization effect. This could be explained by the relatively thick SPE film (250 μm) used in this work. The c-rate test at 30°C was conducted (Figure S13), where the cell exhibited specific capacities of ~123 mAh/g, ~105 mAh/g, ~77 mAh/g, ~55 mAh/g, ~35 mAh/g, and ~122 mAh/g with current densities at 0.2 C, 0.4 C, 0.6 C, 0.2 C, 1 C, and 0.2 C, respectively. The specific capacity differences between

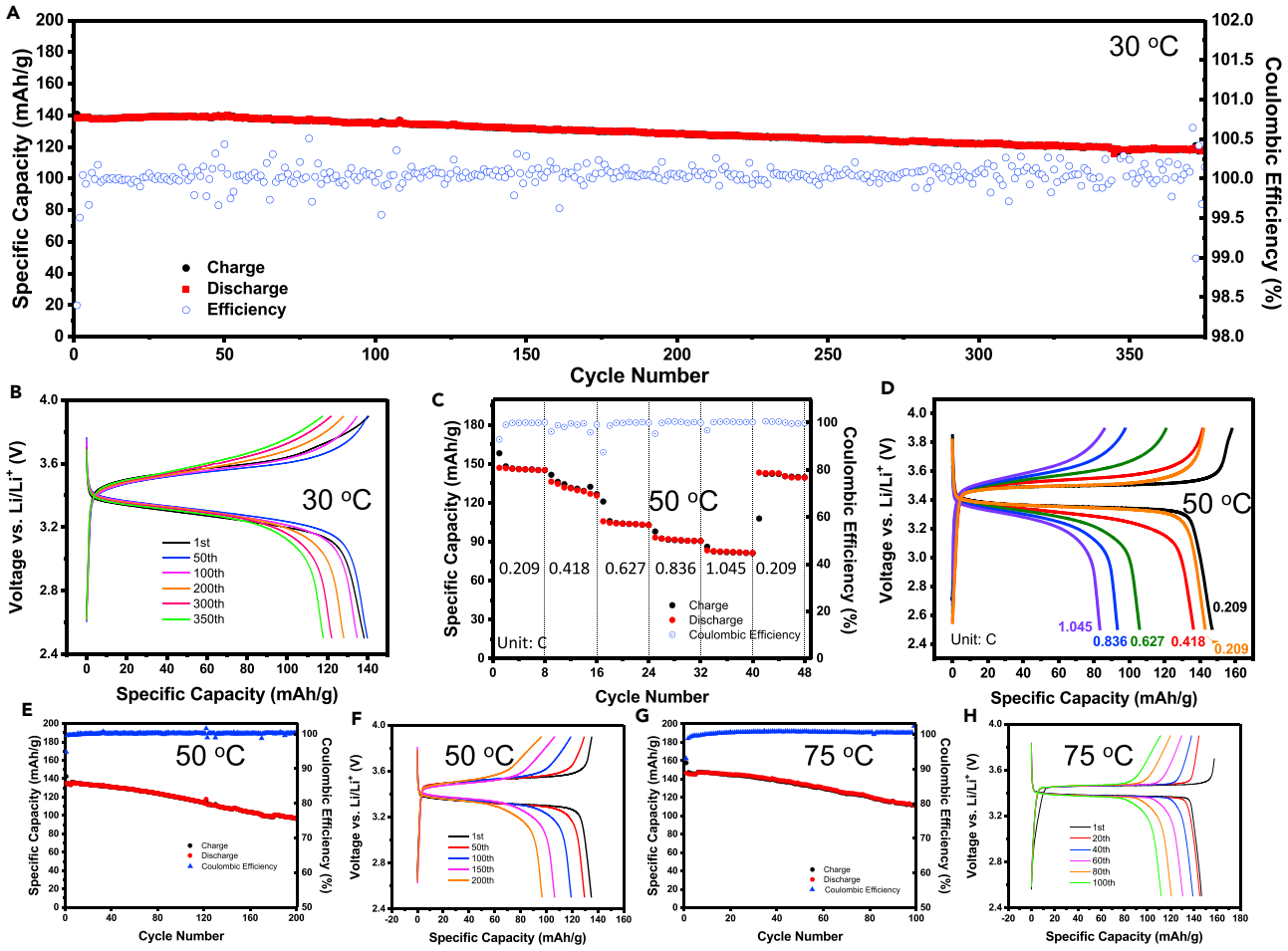

Figure 6. Lithium Battery Testing Results

(A) The cycle performance of DS-SPE-based LIB under 30°C. The initial 10 cycles were operated in the range of 2.5–3.7 V at 0.2 C. The following cycles were operated from 2.5 V to 3.9 V at 0.2 C.

(B) The typical charge/discharge profiles of DS-SPE-based LIB at 30°C.

(C) The ratability test of DS-SPE-based LIB at 50°C from 0.2 C to 1 C.

(D) The charge/discharge profiles of DS-SPE-based LIB at 50°C.

(E) The cycle performance of DS-SPE-based LIB under 50°C.

(F) The typical charge/discharge profiles of DS-SPE-based LIB under 50°C.

(G) The cycle performance of DS-SPE-based LIB under 75°C.

(H) The typical charge/discharge profiles of DS-SPE-based LIB under 75°C.

the ratability test and long-cycling test were likely due to the mass-loading difference of the different batteries. The c-rate performance of the cell was greatly improved when the cell was tested at 50°C (Figures 6C and 6D), where the cell exhibited specific capacities of ~148 mAh/g, ~137 mAh/g, ~108 mAh/g, ~94 mAh/g, ~82 mAh/g, and ~143 mAh/g with current densities at 0.209 C, 0.418 C, 0.627 C, 0.836 C, 1.045 C, and 0.209 C, respectively.

TGA thermogram (Figure 2D) suggested that the SPE could be utilized at elevated temperatures. Therefore, the cell testing was further conducted at elevated temperatures of 50°C and 75°C. At 50°C (Figure 6E), it could be seen that the cell gave an initial specific capacity of 135 mAh/g at a current density of 0.2 C. The cell exhibited a capacity retention of 72% after 200 cycles. The initial specific capacity increased to 147 mAh/g at 75°C (Figure 6G) with a capacity retention of 76% after 100 cycles.

Please cite this article in press as: Li et al., A Superionic Conductive, Electrochemically Stable Dual-Salt Polymer Electrolyte, Joule (2018), https://doi.org/10.1016/j.joule.2018.06.008

From charge/discharge profiles (Figures 6F and 6H), it was apparent that the polarization effect decreased with the increase of temperature, indicating an improvement of power. The c-rate test (Figures 6C and 6D) also confirmed that the power of the cell was greatly enhanced. It was noted that the capacity retention and coulombic efficiency of cells at elevated temperatures (50°C and 75°C) were slightly worse than those at room temperature (30°C), which might be ascribed to the reduced stability of the lithium salts at elevated temperature.[74–76]

Conclusions

The ternary phase diagrams of PEGDA/lithium salt/plasticizer and crosslinked PEGDA/lithium salt/plasticizer were used to guide the design of polymer electrolyte composites. SPE with optimized ionic conductivity over 1.0 mS/cm at 30°C was achieved in the isotropic phase. The free-standing SPE films were flexible and exhibited good thermal stability. The single-salt LiTFSI and dual-salt LiTFSI/LiBOB SPEs were compared in this work. The synergistic effect of the LiTFSI and LiBOB gave the DS-SPE outstanding electrochemical stability: LiBOB protected the aluminum collector, which is susceptible to LiTFSI; LiTFSI mitigated the reaction of LiBOB with lithium metal electrode. The stabilized cathodic and anodic interfaces provided the DS-SPE with a wide chemical window of 0–4.5 V (versus Li/Li^+). The lithium stripping/plating experiments indicated that the SPE could be safely cycled under current densities from 0.05 mA/cm^2 to 0.5 mA/cm^2. The lithium metal cells with free-standing SPE film and infiltrated composite LFP positive electrode were fabricated and tested. The DS-SPE-based cells exhibited outstanding average coulombic efficiency of 99.99% under 30°C in the first 370 cycles. The initial capacity at 30°C was 138 mAh/g (0.2 C), which was close to the value achieved by liquid electrolyte LIB under similar conditions. The capacity retention was 86% after 370 cycles under 0.2 C, indicating the long-term stability of the SPE. At elevated temperatures, the SPE-based cells exhibited enhanced ratability and reduced polarization effect in the charge/discharge profile. This work demonstrated that an optimized ionic conductivity could be achieved by the rational phase diagram approach. By combining a multiple lithium salts strategy, a high electrochemical stability was obtained. The method developed in this work could be expanded to design novel SPEs for advanced lithium metal batteries.

EXPERIMENTAL PROCEDURES

Materials

PEGDA (Sigma Aldrich, 99%) with molecular weight of 700 g/mol, GN ($C_5N_2H_6$, Alfa Aesar, 99%), and photoinitiator *bis*(2,4,6-trimethylbenzoyl)-phenylphosphine oxide (Irgacure 819, Sigma Aldrich, 97%), LiBOB (Sigma Aldrich) were purchased without further purification. LiTFSI (Matrix Scientific), PVDF (HSV900 PVDF, Arkema, >99.5%), and electrode powder material LFP (MTI) were placed in the oven at 100°C overnight to remove residual moisture before use. Battery fabrication components (aluminum current collector and carbon black [Timcal Super P]) were purchased from MTI, anhydrous 1-methyl-2-pyrrolidinone (NMP; Alfa Aesar, 99%), round punched lithium metal pieces (MTI) were used as purchased.

Method to Prepare SPE Film

In a typical fabrication process in making the SPE film, the lithium salts, the prepolymer host PEGDA, and the GN plasticizer were kept and stored in an argon-filled glovebox (O_2 < 0.5 ppm, H_2O < 0.5 ppm). The ternary mixtures with different ratios were used for phase diagram analysis and ionic conductivity study. Due to the relatively small percentage of LiBOB in the SPE, the ternary phase diagram in Figure 1 was obtained by the single-salt system (LiTFSI). All other data (conductivity, TGA,

Please cite this article in press as: Li et al., A Superionic Conductive, Electrochemically Stable Dual-Salt Polymer Electrolyte, Joule (2018), https://doi.org/10.1016/j.joule.2018.06.008

DSC) were obtained by using the DS-SPE. DS-SPEs were used in all electrochemical studies and battery testing unless SS-SPEs were used for comparison. The optimized ratio of the ternary mixture PEGDA/GN/lithium salt was 35:35:30, which was used for all electrochemical testing and battery fabrication. PEGDA and GN were mixed at the given ratio prior to the addition of the LiTFSI salt. The ternary-component blend was vigorously stirred for 30 min at room temperature with a vortex mixer (120 V, VWR International) to obtain a transparent homogeneous solution. LiBOB salt at 2 wt% in respect to the whole solution was subsequently added and heated for 24 hr allowing the salt to be completely dissolved. Irgacure 819 photoinitiator at 1 wt% in respect to the PEGDA was introduced into the transparent homogeneous blend, and then the mixture was further stirred for another 5 min. The transparent mixture was left to rest for 10 min in order to allow the bubbles to defoam. Subsequently, the mixture was poured into a mold with desired depths of thickness with a glass cover on top to obtain a smooth surface and a controlled thickness. A UV light source with a wavelength of 350 nm (25 W Mineralight, UVP) was exposed to the sample for 1 min to obtain a transparent, solvent-free, free-standing SPE film. The light intensity was measured as 0.02 mW/cm^2.

SPE Thermal Analysis

Glass transition temperature and crystallinity of the SPE film was determined by the utilization of DSC (TA Q200, TA Instruments), where the temperature range was scanned from −80°C to 60°C at a temperature ramping rate of 10°C/min. The SPE film samples for the DSC were pre-dried overnight in a dry box prior to the measurements. TGA (TA Q50, TA Instruments) was used to determine the weight percentage component of the ternary system and the thermal stability of the SPE. The temperature was measured from room temperature to 500°C at a rate of 10°C/min under nitrogen atmosphere to validate the weight percentages of different components.

SPE Electrochemical Characterization

Ionic conductivity measurements were carried out by using the stainless steel (StSt)|SPE|StSt configuration. The thickness of the SPE was controlled to 1 mm by using a mold. The thickness of the SPE film was further validated through the use of a thickness gauge (547S-401, Mitutoyo). AC impedance was carried out by using the electrochemical workstation (CHI608E Electrochemical Analyzer, CH Instruments), where the EIS test was scanned in the range of 0.1 Hz–100 kHz with a perturbation voltage of 5 mV. Ionic conductivity at different temperatures was carried out under the same cell configuration but placed in an isothermal chamber. Several data points were collected within the temperature range of −40°C to 100°C. For instance, at 30°C, the cell was placed in the thermal chamber and allowed to rest for at least 30 min prior to conducting the AC impedance. LSV was tested under the StSt|SPE|Li block cell configuration using the same electrochemical workstation under room temperature conditions. The thickness of the SPE film is 1 mm with a diameter of 11 mm. In the LSV, the potential ranges from 0 V to 5.5 V at a sweeping rate of 0.5 mV/s. The same block cell configuration was used for the CV measurements, where the voltage range was selected to be from −0.5 V to 4.8 V at a scanning rate of 0.5 mV/s. In the stripping/plating experiments, symmetric cells (Li|SPE|Li) were fabricated, and the cells were cycled under different current densities for a fixed period of time. In lithium transference number measurement, symmetric cells (Li|SPE|Li) were used. The potentiostatic polarization experiments were conducted with an applied voltage of 10 mV and a polarization time of 10,000 s. The interfacial impedances were measured in the frequency range of 0.1 Hz–100 kHz.

ATR-FTIR, XPS, and Scanning Electron Microscopy Characterization

The XPS spectra were obtained using a VersaProbe II Scanning XPS Microprobe from Physical Electronics (PHI), under ultrahigh vacuum conditions with a pressure of 2×10^{-6} Pa. Automated dual beam charge neutralization was used during the analysis of the samples to provide accurate data. The analyzer pass energy was 117.4 eV for the survey spectra and 11.75 eV for the high-resolution scans in the F1s and C1s regions. The survey scans in the range 0–900 eV were used to evaluate the percentage of different atoms present on the surface of the samples. Atomic concentrations were calculated with PHI MultiPak software. The XPS high-resolution spectra of F1s and C1s were decomposed into components by using the curve fitting routine in MultiPak. Each spectrum was collected using a monochromatic (Al Kα) X-ray beam (E = 1,486.6 eV) over a 100 μm diameter probing area with a beam power of 25 W. ATR-FTIR was conducted on Thermo Scientific Nicolet 6700 FT-IR, using ZnSe prism and scan number of 32. Scanning electron microscopy images were obtained using a Joel 7401 field emission scanning electron microscope.

Lithium Metal Battery Fabrication and Interface Morphology Characterization

Lithium iron phosphate, carbon black, and PVDF were first measured at weight ratios of 80, 10, and 10, respectively. The powders were placed in a Teflon container with ceramic balls and NMP solvent to form the slurry. The container was then placed on a ball milling machine (MTI) to allow vigorous mixing and form a homogeneous thick mixture. The slurry was then cast on an Al foil using a doctor blade to form a layer of coating and then dried at 80°C overnight in an oven to allow the removal of solvents. The electrode was punched into 7.9-mm (5/16 in) circular discs with active material mass loading of approximately 2.5–3.0 mg/cm^2. The electrodes were soaked in the liquid precursor electrolyte without photoinitiator overnight. Then, a fresh free-standing SPE film was laminated on the top of the soaked electrode. The electrode with SPE film was then exposed to UV light to polymerize the liquid into dry SPE. A Li foil was then placed on top of the SPE to give the configuration of Li|SPE|LFP. Scanning electron microscopy images of the SPE cathode interface were obtained by using a JEOL-7401 field emission scanning electron microscope.

Electrochemical Characterization of Lithium Metal Battery

The galvanostatic charge/discharge cycle stability test for the LFP-composite electrode was carried out on an eight-channel battery analyzer (BST-8A; 5 V, 1 mA) from MTI. The initial nine cycles had a potential window of 2.5 V–3.7 V (versus Li/Li$^+$) followed by the potential window of 2.5 V–3.9 V (versus Li/Li$^+$) for the rest of the cycles. The long cycle current density was set to be 0.2 C (in respect to the theoretical capacity of LFP of 175 mAh/g). The cell was further conducted at elevated temperature of 50°C and 75°C, with the same galvanostatic charge/discharge testing conditions.

SUPPLEMENTAL INFORMATION

Supplemental Information includes 13 figures and one table and can be found with this article online at https://doi.org/10.1016/j.joule.2018.06.008.

ACKNOWLEDGMENTS

The authors thank Dr. B. Wang for the help with the scanning electron microscopy. The authors would like to thank Edwards Laughlin for the assistance in fabricating and designing the heating oven. The authors would like to thank Jiawei Liu for the ATR-FTIR experiments. We acknowledge the use of VersaProbe II XPS Microprobe in the Surface and Optical Analysis Facility of the National Polymer Innovation

Center in the College of Polymer Science and Engineering. The authors are grateful for financial support from the National Science Foundation (NSF) through NSF-CBET 1505943, 1706681, and NSF-DMR 1554851, and Ohio Federal Network Research (OFRN) through the Center of Excellence (WSARC-1077-100).

AUTHOR CONTRIBUTIONS

Y.Z. conceived and designed the study. S.L. and Y.-M.C. performed the experiments on material synthesis, characterization, and battery testing. W.L. and Y.S. contributed to the electrochemical test and FTIR experiments. K.L. and Z.N. contributed to the XPS experiments. S.L., Y.-M.C., and Y.Z. prepared the manuscript. S.L. and Y.-M.C. contributed equally to the work. All authors discussed the results and commented on the manuscript.

DECLARATION OF INTERESTS

Y.Z. declares a provisional patent application (USPTO 62/515,000) owned by University of Akron that discloses the high ionic conductivity SPE composite.

Received: January 22, 2018
Revised: May 1, 2018
Accepted: June 5, 2018
Published: June 26, 2018

REFERENCES

1. Armand, M., and Tarascon, J.M. (2008). Building better batteries. Nature *451*, 652–657.
2. Scrosati, B., and Garche, J. (2010). Lithium batteries: status, prospects and future. J. Power Sources *195*, 2419–2430.
3. Heller, A. (2013). The GS Yuasa-Boeing 787 Li-ion battery: test it at a low temperature and keep it warm in flight. Electrochem. Soc. Interface *22*, 35.
4. Tarascon, J.M., and Armand, M. (2001). Issues and challenges facing rechargeable lithium batteries. Nature *414*, 359–367.
5. Aurbach, D., Zinigrad, E., Cohen, Y., and Teller, H. (2002). A short review of failure mechanisms of lithium metal and lithiated graphite anodes in liquid electrolyte solutions. Solid State Ion. *148*, 405–416.
6. Goodenough, J.B., and Kim, Y. (2010). Challenges for rechargeable Li batteries. Chem. Mater. *22*, 587–603.
7. Xu, W., Wang, J., Ding, F., Chen, X., Nasybulin, E., Zhang, Y., and Zhang, J.-G. (2014). Lithium metal anodes for rechargeable batteries. Energy Environ. Sci. *7*, 513–537.
8. Sun, Y., Liu, N., and Cui, Y. (2016). Promises and challenges of nanomaterials for lithium-based rechargeable batteries. Nat. Energy *1*, 16071.
9. Lin, D., Liu, Y., and Cui, Y. (2017). Reviving the lithium metal anode for high-energy batteries. Nat. Nanotechnol. *12*, 194–206.
10. Bruce, P.G., Freunberger, S.A., Hardwick, L.J., and Tarascon, J.-M. (2012). Li-O2 and Li-S batteries with high energy storage. Nat. Mater. *11*, 19–29.
11. Manthiram, A., Fu, Y., Chung, S.-H., Zu, C., and Su, Y.-S. (2014). Rechargeable lithium–sulfur batteries. Chem. Rev. *114*, 11751–11787.
12. Luntz, A.C., and McCloskey, B.D. (2014). Nonaqueous Li–air batteries: a status report. Chem. Rev. *114*, 11721–11750.
13. Manthiram, A., Yu, X., and Wang, S. (2017). Lithium battery chemistries enabled by solid-state electrolytes. Nat. Rev. Mater. *2*, 16103.
14. Hassoun, J., and Scrosati, B. (2010). Moving to a solid-state configuration: a valid approach to making lithium-sulfur batteries viable for practical applications. Adv. Mater. *22*, 5198–5201.
15. Goodenough, J.B., and Singh, P. (2015). Review-solid electrolytes in rechargeable electrochemical cells. J. Electrochem. Soc. *162*, A2387–A2392.
16. Xu, K. (2004). Nonaqueous liquid electrolytes for lithium-based rechargeable batteries. Chem. Rev. *104*, 4303–4418.
17. Xu, K. (2014). Electrolytes and interphases in Li-ion batteries and beyond. Chem. Rev. *114*, 11503–11618.
18. Yue, L.P., Ma, J., Zhang, J.J., Zhao, J.W., Dong, S.M., Liu, Z.H., Cui, G.L., and Chen, L.Q. (2016). All solid-state polymer electrolytes for high-performance lithium ion batteries. Energy Storage Mater. *5*, 139–164.
19. Cui, Y.Y., Chai, J.C., Du, H.P., Duan, Y.L., Xie, G.W., Liu, Z.H., and Cui, G.L. (2017). Facile and reliable in situ polymerization of poly(ethyl cyanoacrylate)-based polymer electrolytes toward flexible lithium batteries. ACS Appl. Mater. Interfaces *9*, 8737–8741.
20. Wright, P.V. (1975). Electrical conductivity in ionic complexes of poly(ethylene oxide). Br. Polym. J. *7*, 319–327.
21. Armand, M.B., Chabagno, J.M., and Duclot, M. (1979). Poly-ethers as solid electrolytes. In Fast Ion Transport in Solids: Electrodes and Electrolytes, P. Vashitshta, J.N. Mundy, and G.K. Shenoy, eds. (North-Holland).
22. Feuillade, G., and Perche, P. (1975). Ion-conductive macromolecular gels and membranes for solid lithium cells. J. Appl. Electrochem. *5*, 63–69.
23. Rajendran, S., Babu, R.S., and Sivakumar, P. (2008). Ionic conduction in plasticized PVC/PAN blend polymer electrolytes. Ionics *14*, 149–155.
24. Lewandowski, A., and Majchrzak, I. (1997). Polyacrylonitrile-DMSO-AgClO4 solid polymer electrolyte. Electrochim. Acta *42*, 267–270.
25. Appetecchi, G.B., Croce, F., and Scrosati, B. (1995). Kinetics and stability of the lithium electrode in poly(methylmethacrylate)-based gel electrolytes. Electrochim. Acta *40*, 991–997.
26. Stephan, A.M., Renganathan, N.G., Kumar, T.P., Thirunakaran, R., Pitchumani, S., Shrisudersan, J., and Muniyandi, N. (2000). Ionic conductivity studies on plasticized PVC/PMMA blend polymer electrolyte containing $LiBF_4$ and $LiCF_3SO_3$. Solid State Ion. *130*, 123–132.
27. Manuel Stephan, A., Gopu Kumar, S., Renganathan, N.G., and Anbu Kulandainathan, M. (2005). Characterization of poly(vinylidene fluoride–hexafluoropropylene) (PVdF–HFP) electrolytes complexed with different lithium salts. Eur. Polym. J. *41*, 15–21.

28. Mary Sukeshini, A., Nishimoto, A., and Watanabe, M. (1996). Transport and electrochemical characterization of plasticized poly(vinyl chloride) solid electrolytes. Solid State Ion. *86–88* (Part 1), 385–393.

29. Alamgir, M., and Abraham, K.M. (1993). Li ion conductive electrolytes based on poly(vinyl chloride). J. Electrochem. Soc. *140*, L96–L97.

30. Gorecki, W., Jeannin, M., Belorizky, E., Roux, C., and Armand, M. (1995). Physical properties of solid polymer electrolyte PEO(LiTFSI) complexes. J. Phys. Condens. Matter *7*, 6823.

31. Karan, N.K., Pradhan, D.K., Thomas, R., Natesan, B., and Katiyar, R.S. (2008). Solid polymer electrolytes based on polyethylene oxide and lithium trifluoro- methane sulfonate ($PEO–LiCF_3SO_3$): ionic conductivity and dielectric relaxation. Solid State Ion. *179*, 689–696.

32. Armand, M., Gorecki, W., and Andreani, R. (1990). Proceedings in the Second International Meeting on Polymer Electrolytes (Elsevier).

33. Gray, F.M. (1991). Solid Polymer Electrolytes: Fundamentals and Technological Applications (VCH).

34. Buriez, O., Han, Y.B., Hou, J., Kerr, J.B., Qiao, J., Sloop, S.E., Tian, M., and Wang, S. (2000). Performance limitations of polymer electrolytes based on ethylene oxide polymers. J. Power Sources *89*, 149–155.

35. Rietman, E.A., Kaplan, M.L., and Cava, R.J. (1985). Lithium ion-poly (ethylene oxide) complexes. I. Effect of anion on conductivity. Solid State Ion. *17*, 67–73.

36. Dias, F.B., Plomp, L., and Veldhuis, J.B.J. (2000). Trends in polymer electrolytes for secondary lithium batteries. J. Power Sources *88*, 169–191.

37. Meyer, W.H. (1998). Polymer electrolytes for lithium-ion batteries. Adv. Mater. *10*, 439–448.

38. Berthier, C., Gorecki, W., Minier, M., Armand, M.B., Chabagno, J.M., and Rigaud, P. (1983). Microscopic investigation of ionic conductivity in alkali metal salts-poly(ethylene oxide) adducts. Solid State Ion. *11*, 91–95.

39. Wang, Y., and Zhong, W.-H. (2015). Development of electrolytes towards achieving safe and high-performance energy-storage devices: a review. ChemElectroChem *2*, 22–36.

40. Staunton, E., Andreev, Y.G., and Bruce, P.G. (2007). Factors influencing the conductivity of crystalline polymer electrolytes. Faraday Discuss *134*, 143–156.

41. Qian, X., Gu, N., Cheng, Z., Yang, X., Wang, E., and Dong, S. (2002). Plasticizer effect on the ionic conductivity of PEO-based polymer electrolyte. Mater. Chem. Phys. *74*, 98–103.

42. Ramesh, S., and Ling, O.P. (2010). Effect of ethylene carbonate on the ionic conduction in poly(vinylidenefluoride-hexafluoropropylene) based solid polymer electrolytes. Polym. Chem. *1*, 702–707.

43. Das, S., and Ghosh, A. (2015). Effect of plasticizers on ionic conductivity and dielectric relaxation of PEO-LiClO4 polymer electrolyte. Electrochim. Acta *171*, 59–65.

44. Alarco, P.-J., Abu-Lebdeh, Y., Abouimrane, A., and Armand, M. (2004). The plastic-crystalline phase of succinonitrile as a universal matrix for solid-state ionic conductors. Nat. Mater. *3*, 476–481.

45. Wu, X.-L., Xin, S., Seo, H.-H., Kim, J., Guo, Y.-G., and Lee, J.-S. (2011). Enhanced Li+ conductivity in PEO–LiBOB polymer electrolytes by using succinonitrile as a plasticizer. Solid State Ion. *186*, 1–6.

46. Fan, L.-Z., and Maier, J. (2006). Composite effects in poly(ethylene oxide)–succinonitrile based all-solid electrolytes. Electrochem. Commun. *8*, 1753–1756.

47. Quartarone, E., and Mustarelli, P. (2011). Electrolytes for solid-state lithium rechargeable batteries: recent advances and perspectives. Chem. Soc. Rev. *40*, 2525–2540.

48. Rey, I., Lassègues, J.C., Grondin, J., and Servant, L. (1998). Infrared and Raman study of the PEO-LiTFSI polymer electrolyte. Electrochim. Acta *43*, 1505–1510.

49. Bakker, A., Gejji, S., Lindgren, J., Hermansson, K., and Probst, M.M. (1995). Contact ion pair formation and ether oxygen coordination in the polymer electrolytes $M[N(CF_3SO_2)_2]_2PEO_n$ for M = Mg, Ca, Sr and Ba. Polymer *36*, 4371–4378.

50. Gorecki, W., Roux, C., Clemancey, M., Armand, M., and Belorizky, E. (2002). NMR and conductivity study of polymer electrolytes in the imide family: P(EO)/Li $[N(SO_2C_nF_{2n+1})(SO_2C_mF_{2m+1})]$. Chemphyschem *3*, 620–625.

51. Mao, G., Saboungi, M.L., Price, D.L., Armand, M.B., and Howells, W.S. (2000). Structure of liquid PEO-LiTFSI electrolyte. Phys. Rev. Lett. *84*, 5536–5539.

52. He, R., Echeverri, M., Ward, D., Zhu, Y., and Kyu, T. (2016). Highly conductive solvent-free polymer electrolyte membrane for lithium-ion batteries: effect of prepolymer molecular weight. J. Membr. Sci. *498*, 208–217.

53. Keim, T., and Gall, K. (2010). Synthesis, characterization, and cyclic stress-influenced degradation of a poly(ethylene glycol)-based poly(beta-amino ester). J. Biomed. Mater. Res. A *92A*, 702–711.

54. Arbizzani, C., Gabrielli, G., and Mastragostino, M. (2011). Thermal stability and flammability of electrolytes for lithium-ion batteries. J. Power Sources *196*, 4801–4805.

55. Bruce, P.G., Evans, J., and Vincent, C.A. (1988). Conductivity and transference number measurements on polymer electrolytes. Solid State Ion. *28*, 918–922.

56. Schaefer, J.L., Yanga, D.A., and Archer, L.A. (2013). High lithium transference number electrolytes via creation of 3-dimensional, charged, nanoporous networks from dense functionalized nanoparticle composites. Chem. Mater. *25*, 834–839.

57. Zhou, W., Wang, S., Li, Y., Xin, S., Manthiram, A., and Goodenough, J.B. (2016). Plating a dendrite-free lithium anode with a polymer/ceramic/polymer sandwich electrolyte. J. Am. Chem. Soc. *138*, 9385–9388.

58. Zheng, J., Engelhard, M.H., Mei, D., Jiao, S., Polzin, B.J., Zhang, J.-G., and Xu, W. (2017). Electrolyte additive enabled fast charging and stable cycling lithium metal batteries. Nat. Energy *2*, 17012.

59. Monroe, C., and Newman, J. (2005). The impact of elastic deformation on deposition kinetics at lithium/polymer interfaces. J. Electrochem. Soc. *152*, A396–A404.

60. Sun, B., Xu, C., Mindemark, J., Gustafsson, T., Edstrom, K., and Brandell, D. (2015). At the polymer electrolyte interfaces: the role of the polymer host in interphase layer formation in Li-batteries. J. Mater. Chem. A *3*, 13994–14000.

61. Yang, X.D., Li, J., Liu, J., Tian, Y., Li, B., Cao, K.C., Liu, S.B., Hou, M., Li, S.J., and Ma, L.J. (2014). Simple small molecule carbon source strategy for synthesis of functional hydrothermal carbon: preparation of highly efficient uranium selective solid phase extractant. J. Mater. Chem. A *2*, 1550–1559.

62. Li, X., Zheng, J.M., Engelhard, M.H., Mei, D.H., Li, Q.Y., Jiao, S.H., Liu, N., Zhao, W.G., Zhang, J.G., and Xu, W. (2018). Effects of imide-orthoborate dual-salt mixtures in organic carbonate electrolytes on the stability of lithium metal batteries. ACS Appl. Mater. Interfaces *10*, 2469–2479.

63. Sharova, V., Moretti, A., Diemant, T., Varzi, A., Behm, R.J., and Passerini, S. (2018). Comparative study of imide-based Li salts as electrolyte additives for Li-ion batteries. J. Power Sources *375*, 43–52.

64. Zhu, Y., Li, X.Y., Cai, Q.J., Sun, Z.Z., Casillas, G., Jose-Yacaman, M., Verduzco, R., and Tour, J.M. (2012). Quantitative analysis of structure and bandgap changes in graphene oxide nanoribbons during thermal annealing. J. Am. Chem. Soc. *134*, 11774–11780.

65. Carey, F.A., and Giuliano, R.M. (2016). Organic Chemistry, Tenth Edition (McGraw-Hill Education).

66. Elschenbroich, C. (2006). Organometallics (Wiley-VCH), 3rd, completely rev. and extended edn.

67. Parker, V.D. (1973). The anodic oxidation of hydroquinone in acetonitrile. On the question of a possible one electron intermediate. Electrochim. Acta *18*, 519–524.

68. Nie, M.Y., Abraham, D.P., Chen, Y.J., Bose, A., and Lucht, B.L. (2013). Silicon solid electrolyte interphase (SEI) of lithium ion battery characterized by microscopy and spectroscopy. J. Phys. Chem. C *117*, 13403–13412.

69. Veith, G.M., Doucet, M., Sacci, R.L., Vacaliuc, B., Baldwin, J.K., and Browning, J.F. (2017). Determination of the solid electrolyte interphase structure grown on a silicon electrode using a fluoroethylene carbonate additive. Sci. Rep. *7*, 6326.

70. Wu, B., Wang, S., Evans Iv, W.J., Deng, D.Z., Yang, J., and Xiao, J. (2016). Interfacial behaviours between lithium ion conductors and electrode materials in various battery systems. J. Mater. Chem. A *4*, 15266–15280.

71. Abe, T., Ohtsuka, M., Sagane, F., Iriyama, Y., and Ogumi, Z. (2004). Lithium ion transfer at

the interface between lithium-ion-conductive solid crystalline electrolyte and polymer electrolyte. J. Electrochem. Soc. *151*, A1950–A1953.

72. Tenhaeff, W.E., Yu, X., Hong, K., Perry, K.A., and Dudney, N.J. (2011). Ionic transport across interfaces of solid glass and polymer electrolytes for lithium ion batteries. J. Electrochem. Soc. *158*, A1143–A1149.

73. Zhang, H., Liu, C., Zheng, L., Xu, F., Feng, W., Li, H., Huang, X., Armand, M., Nie, J., and Zhou, Z. (2014). Lithium bis(fluorosulfonyl)imide/poly(ethylene oxide) polymer electrolyte. Electrochim. Acta *133*, 529–538.

74. Xu, K., Lee, U., Zhang, S., Wood, M., and Jow, T.R. (2003). Chemical analysis of graphite/electrolyte interface formed in LiBOB-based electrolytes. Electrochem. Solid State Lett. *6*, A144–A148.

75. Xu, K., Zhang, S., Jow, T.R., Xu, W., and Angell, C.A. (2002). LiBOB as salt for lithium-ion batteries: a possible solution for high temperature operation. Electrochem. Solid State Lett. *5*, A26–A29.

76. Sloop, S.E., Pugh, J.K., Wang, S., Kerr, J.B., and Kinoshita, K. (2001). Chemical reactivity of PF5 and LiPF6 in ethylene carbonate/dimethyl carbonate solutions. Electrochem. Solid State Lett. *4*, A42–A44.